

# Single-crystal hBN Monolayers from Aligned Hexagonal Islands

Received: 13 September 2024

Accepted: 26 September 2024

Published online: 04 October 2024

 Check for updates

Junzhu Li<sup>1,2</sup>, Abdus Samad<sup>1</sup>, Yue Yuan<sup>1</sup>, Qingxiao Wang<sup>3</sup>,  
Mohamed Nejib Hedhili<sup>3</sup>, Mario Lanza<sup>1</sup>, Udo Schwingenschlögl<sup>1</sup>,  
Iwnetim Abate<sup>4</sup>, Deji Akinwande<sup>5</sup>, Zheng Liu<sup>2</sup>, Bo Tian<sup>2</sup>✉ &  
Xixiang Zhang<sup>1</sup>✉

Hexagonal boron nitride (hBN), as one of the few two-dimensional insulators, holds strategic importance for advancing post-silicon electronic devices and circuits. Achieving wafer-scale, high-quality monolayer hBN is essential for its integration into the semiconductor industry. However, the physical mechanisms behind the chemical vapor deposition (CVD) synthesis of hBN are not yet well understood. Investigating morphology engineering is critical for developing scalable synthetic techniques for the large-scale production of high-quality hBN. In this study, we explored the underlying mechanisms of the CVD growth process of hBN and found that the involvement of a small amount of oxygen effectively modulates the shape of the single-crystal hBN islands. By tuning the oxygen content in the CVD system, we synthesized well-aligned hexagonal hBN islands and achieved a continuous, high-quality single-crystal monolayer hBN film through the merging of these hexagonal islands on conventional single-crystal metal-foil substrates. Density functional theory was used to study the edges of hBN monolayers grown in an oxygen-assisted environment, providing insights into the formation mechanism. This study opens new pathways for controlling the island shape of 2D materials and establishes a foundation for the industrial-scale production of high-quality, large-area, single-crystal hBN.

As an insulating two-dimensional (2D) layered material, hexagonal boron nitride (hBN) has attracted considerable interest from the scientific community because of its unique physical and chemical properties that differ from those of other 2D materials, such as graphene and transition-metal dichalcogenides<sup>1–3</sup>. In recent years, hBN-based van der Waals heterostructures, in combination with other 2D materials, have shown promising applications in magic-angle systems, superconductivity studies, and neuromorphic nanodevices<sup>4–11</sup>. However, most of these applications are based on hBN flakes that are

mechanically exfoliated from bulk materials. The production of large-area, high-quality, single-crystal hBN film via chemical vapor deposition (CVD) is critical for its future applications. Significant research has been conducted by materials scientists on the CVD synthesis of hBN films over the past decades, and large-area hBN monolayers and multilayers formed by merging traditional triangle-shaped hBN islands have been grown on Cu and Ni substrates<sup>12–29</sup>. Notably, wafer-scale single-crystal hBN films have been achieved by merging mono-oriented triangular hBN islands grown on twin-grain-free Cu(111)

<sup>1</sup>Physical Science and Engineering Division, King Abdullah University of Science and Technology (KAUST), Thuwal 23955-6900, Saudi Arabia. <sup>2</sup>School of Materials Science and Engineering, Nanyang Technological University, 50 Nanyang Avenue, Singapore 639798, Singapore. <sup>3</sup>Imaging and Characterization Core Lab, King Abdullah University of Science and Technology (KAUST), Thuwal 23955-6900, Saudi Arabia. <sup>4</sup>Department of Materials Science and Engineering, Massachusetts Institute of Technology, Cambridge, MA 02139, USA. <sup>5</sup>Microelectronics Research Center, The University of Texas at Austin, Austin, TX 78758, USA. ✉e-mail: [botianlab@gmail.com](mailto:botianlab@gmail.com); [xixiang.zhang@kaust.edu.sa](mailto:xixiang.zhang@kaust.edu.sa)

films on single-crystal sapphire substrates<sup>14</sup>. However, the synthesis of large-area, high-quality monolayer hBN through morphology engineering of well-aligned, hexagonal-shaped islands has yet to be realized.

Herein, we report the successful growth of high-quality single-crystal monolayer hBN films on Cu(111) foils by merging the well-aligned, unconventional hexagonal-shaped hBN islands. Based on the investigation of growth mechanisms and energy states of various edges in hBN islands, we found that the involvement of a small amount of oxygen can affect the energies of B- and N-terminated edges during the CVD growth of hBN, which consequently influences the morphology of the so-formed hBN islands. Different characterization results confirmed the high crystal quality, excellent dielectric properties, uniform layer thickness, and single crystallinity of the as-grown hBN monolayers. Furthermore, hBN islands with different edges under both conventional and oxygen-assisted environments were investigated using density functional theory (DFT) simulations, which supported our experimental observations. This study presents a novel approach for synthesizing unconventional graphene-like hexagonal hBN islands, in contrast to the commonly observed triangular islands. In addition, it highlights the potential of large-area, premium-quality monolayer hBN films for future post-silicon applications.

## Results and discussion

### Hexagonal-shaped hBN islands

In contrast to the  $C_{6v}$  crystal symmetry of graphene, hBN islands mostly exhibit a lower three-fold crystal symmetry ( $C_{3v}$ ), attributed to the alternating arrangement of boron (B) and nitrogen (N) atoms in the honeycomb lattice of hBN<sup>30,31</sup>. This crystal structure suggests that triangular hBN islands, rather than hexagonal islands, are the most stable configuration on metal substrates (Fig. 1a). We modified the island shape during the hBN CVD growth by manipulating the energy difference of B- and N-terminated edges. Our findings reveal that oxygen alters the difference in edge energies, resulting in nearly identical growth rates for both edges. Consequently, this leads to the formation of unconventional hexagonal-shaped hBN islands instead of the commonly observed triangular ones (Fig. 1b, c).

In the traditional CVD synthesis of hBN, ammonia borane is thermally decomposed and introduced into the high-temperature reaction chamber, along with an argon carrier gas, to form the hBN film under the catalysis of Cu substrates (Supplementary Fig. 1). As previously discussed, triangular islands are commonly observed in hBN growth on the Cu(111) surface (Fig. 2a). However, in this study, we experimentally discovered that introducing a small amount of oxygen (diluted in argon) into the chamber during CVD growth results in the formation of hBN islands with an unconventional hexagonal shape, instead of the typical triangular (Fig. 2b). By adjusting the CVD growth parameters, hBN islands with hexagonal shapes – similar to the shapes of graphene islands in typical cases<sup>32–35</sup>, were achieved on the single-crystal Cu(111) foil. Scanning electron microscopy (SEM) analysis

revealed that the hBN islands grown using the oxygen-assisted CVD strategy exhibit a consistent hexagonal shape, and all of them aligned in the same direction (Fig. 2c and Supplementary Fig. 2).

To directly observe the morphology of as-grown hBN islands, the sample was heated on a hot plate (150 °C for 2 min) in air, leading to the oxidation of the Cu surface in the areas without coverage of hBN into colored  $\text{CuO}_x$ , while the area covered by the hBN island was protected from oxidation. This process enabled easier observation of the hBN island using optical microscopy. Owing to the strong fluorescence background from the Cu substrate, the extremely weak Raman signals of monolayer hBN could not be detected in the Raman measurements<sup>36–38</sup>. Therefore, we collected the Raman maps of  $\text{CuO}_x$  signals to indirectly observe the triangular and hexagonal shapes of as-grown hBN islands (Fig. 2d, e). The Raman spectra collected on the bare Cu regions show distinct  $\text{CuO}_x$  bands, indicating the Cu oxidation (Fig. 2f). In contrast, no  $\text{CuO}_x$  bands were observed in the regions covered by hBN islands, as shown in Fig. 2g.

Atomic force microscopy (AFM) was used to characterize the surface morphology of as-grown triangle- and hexagonal-shaped hBN islands. The hBN surface with visible Cu steps was observed in the region of the hexagonal island (with a surface roughness of 0.50 nm), whereas a rougher and slightly higher surface of  $\text{CuO}_x$  with a surface roughness of 2.26 nm exhibited in the AFM topography map (Fig. 2h and Supplementary Figs. 3 and 4). Conductive AFM (CAFM) was employed to investigate the presence of pinholes by scanning the surface of the hBN films at a low constant voltage of 7.5 mV. At this voltage, CAFM is capable of detecting pinholes without generating a tunneling current across the monolayer hBN film. The current map shows no leakage current across the hexagonal island (Fig. 2i), indicating that the hBN island is free of pinholes. Next, by applying ramped voltage stresses and recording the current versus voltage ( $I$ - $V$ ) curves, we investigated the ability of the monolayer hBN island to block out-of-plane leakage current (i.e., quantum tunneling). We collected  $I$ - $V$  curves at 77 randomly selected positions on 23 hexagonal-shaped hBN islands (Fig. 2j), and repeated the same experiment on triangle-shaped hBN islands (in this case, measuring 66 positions across 13 islands, see Fig. 2k). From the CAFM results, it can be concluded that the as-grown hexagonal hBN islands are of high quality due to the following observations: (i) there are no  $I$ - $V$  curves showing linear current increasing from 0 V, meaning that it has no pinholes, (ii) the minimum voltage that produces current (called onset potential) is  $0.47 \pm 0.14$  V, which is much higher than that observed in commercial monolayer CVD-grown hBN samples, and (iii) the deviation of the onset potential is rather low despite having measured the  $I$ - $V$  curves on multiple different islands (Fig. 2l). In contrast, the triangle-shaped hBN islands exhibit some linear  $I$ - $V$  curves at low potentials, and some highly insulating  $I$ - $V$  curves (Fig. 2m). The overlap of the backward  $I$ - $V$  curves with the forward ones indicates that no degradation occurs in the hexagonal-shaped hBN islands (Supplementary Fig. 5). This further demonstrates the excellent quality of the hexagonal-shaped hBN islands grown in this study.

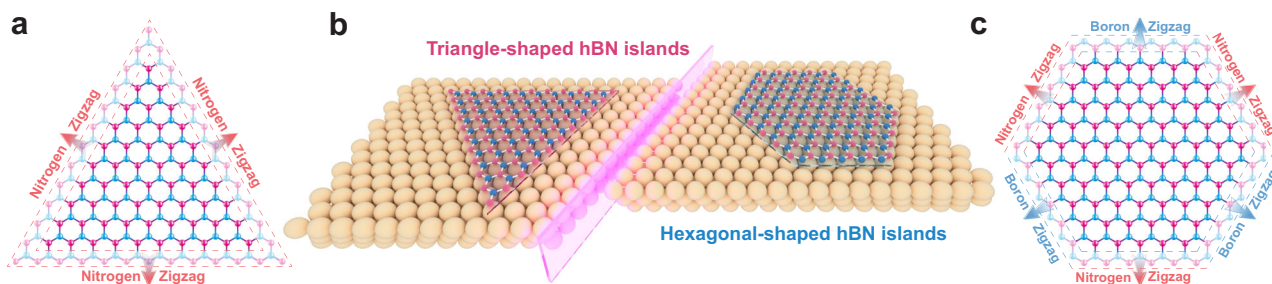


**Fig. 1 | Triangle and hexagonal shapes of hexagonal boron nitride (hBN) islands on Cu(111) substrates. a–c** Atomic illustrations of the triangle-shaped hBN island with all N-terminated edges (a), and the hexagonal-shaped hBN island with the same number of N- and B-terminated edges (c).

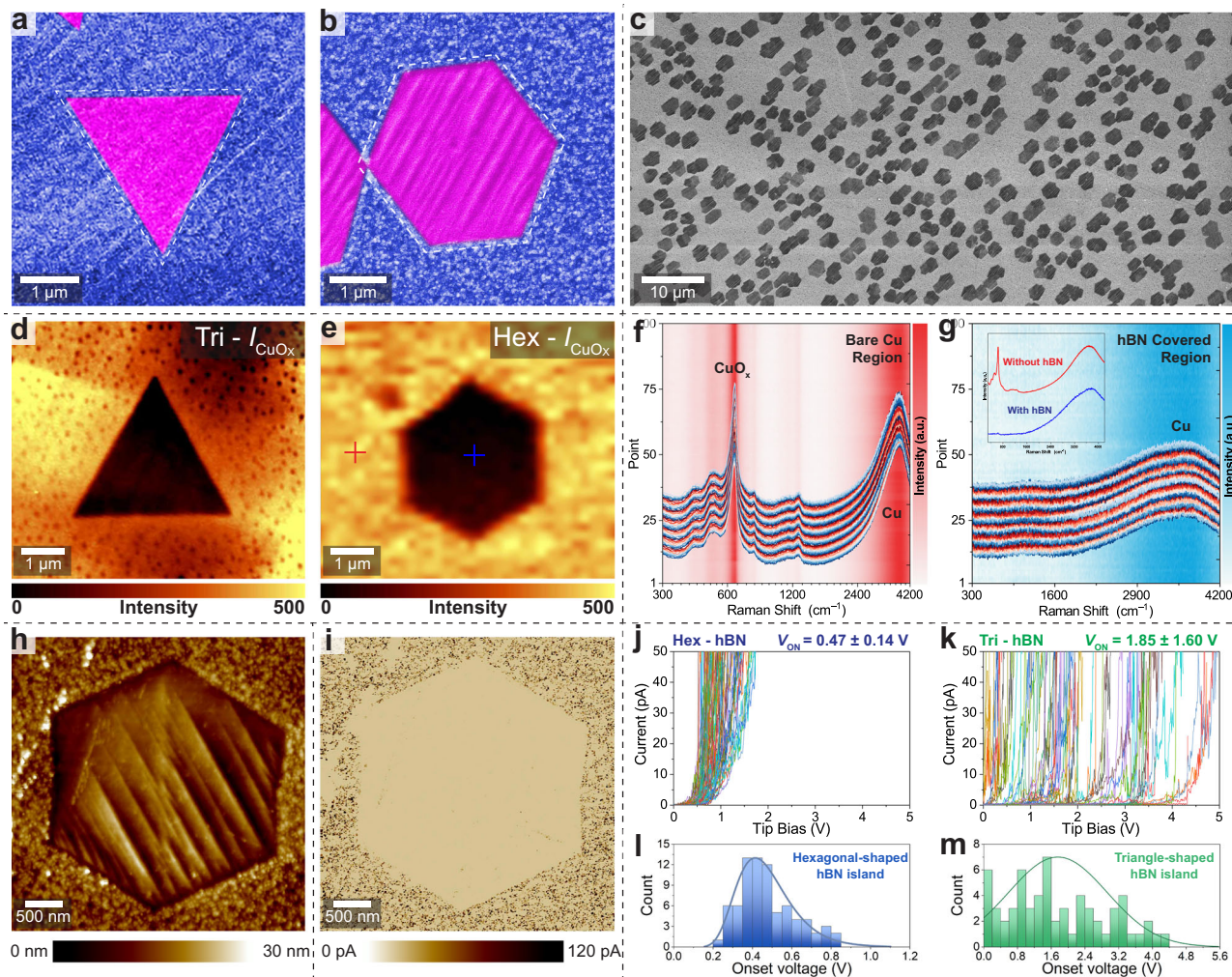


**Fig. 2 | Oxygen-assisted growth of hexagonal-shaped hBN on Cu(111).** **a, b** False-color scanning electron microscopy (SEM) images of as-grown hBN on Cu(111) foils with triangular (**a**) and hexagonal islands (**b**). **c** SEM image of as-grown well-aligned hexagonal-shaped hBN islands on the Cu(111) substrate. **d, e** Raman maps of the  $\text{CuO}_x$  intensity ( $I_{\text{CuO}_x}$ ) measured on the triangle- (**d**) and hexagonal-shaped hBN islands (**e**). **f, g** Raman spectra taken from  $\sim 100$  random locations of bare Cu (**f**) and hBN-covered (**g**) regions. The compared spectra collected from the marked positions in (**e**) are shown in the inset of (**g**). **h, i** Atomic force microscopy (AFM)

topography (**h**) and conductive AFM current map (**i**) of as-grown hexagonal-shaped hBN island on Cu(111) substrate after the oxidation treatment. **j, k**  $I$ - $V$  curves collected from 77 and 66 random positions in the area of as-grown hexagonal- (**j**) and triangle-shaped (**k**) hBN islands on Cu(111) by applying ramped voltage stresses from 0 to 10 V to the tip. **l, m** Statistical analysis of the onset voltages for hexagonal-shaped (**l**) and triangle-shaped (**m**) hBN islands. The solid lines show fitted distribution curves, illustrating the differences in onset voltages between the two island shapes.

### DFT simulations

To further investigate the energetically favorable edge configuration of monolayer hBN and the formation mechanism of triangular and hexagonal hBN islands, DFT simulations were performed. Six stackings of monolayer hBN on Cu(111) were modeled, and the energetically favorable stacking ( $B_{\text{fcc}}N_{\text{top}}$ ) was used for further study (Supplementary Fig. 6). Firstly, we studied freestanding monolayer hBN with zigzag edges (Fig. 3a). The N-terminated edges turned out to be energetically favorable over the B-terminated edges by 312 meV per edge atom. On Cu(111), this difference increased to 959 meV per edge atom (Fig. 3b), revealing that the N-termination becomes even more favorable in the hBN growth. This is due to the fact that the edges of monolayer hBN interact with Cu(111), causing them to bend (Supplementary Fig. 7). Examining the distances between the edge N or B atoms and the closest Cu atoms, an N-Cu distance of 1.90 Å and a B-Cu distance of 2.21 Å were observed for the N-terminated and B-terminated edge, respectively. This difference in the bond length explains why the N-terminated zigzag edge is energetically favorable over the B-terminated zigzag edge on Cu(111). These theoretical results suggest

that hBN forms triangular islands with N-terminated zigzag edges, which is consistent with the experimental observations in the hBN CVD growth.

Furthermore, the effect of low concentrations of oxygen in the hBN CVD growth was studied by DFT simulations (Fig. 3c, d). The oxygen atoms were found to interact with the edge of monolayer hBN and with Cu(111) substrate. The energy difference between the N- and B-terminated edges decreased from 959 meV per edge atom in the absence of oxygen to 21 meV per edge atom, which is even lower than in the case of freestanding hBN (312 meV per edge atom) (Fig. 3e). The fact that N- and B-terminated edges are almost energetically degenerate in the presence of oxygen implies that the probability of formation and existence is close to equal. As a consequence, in the presence of oxygen, no triangular hBN islands (all edges either N- or B-terminated) will form, but rather hexagonal hBN islands with alternating N- and B-terminated edges. In addition, the step-edge guiding mechanism has been reported and widely employed in the growth of single-crystal 2D material films in past studies<sup>13–15</sup>. The surface- and step-edge growth mode configurations

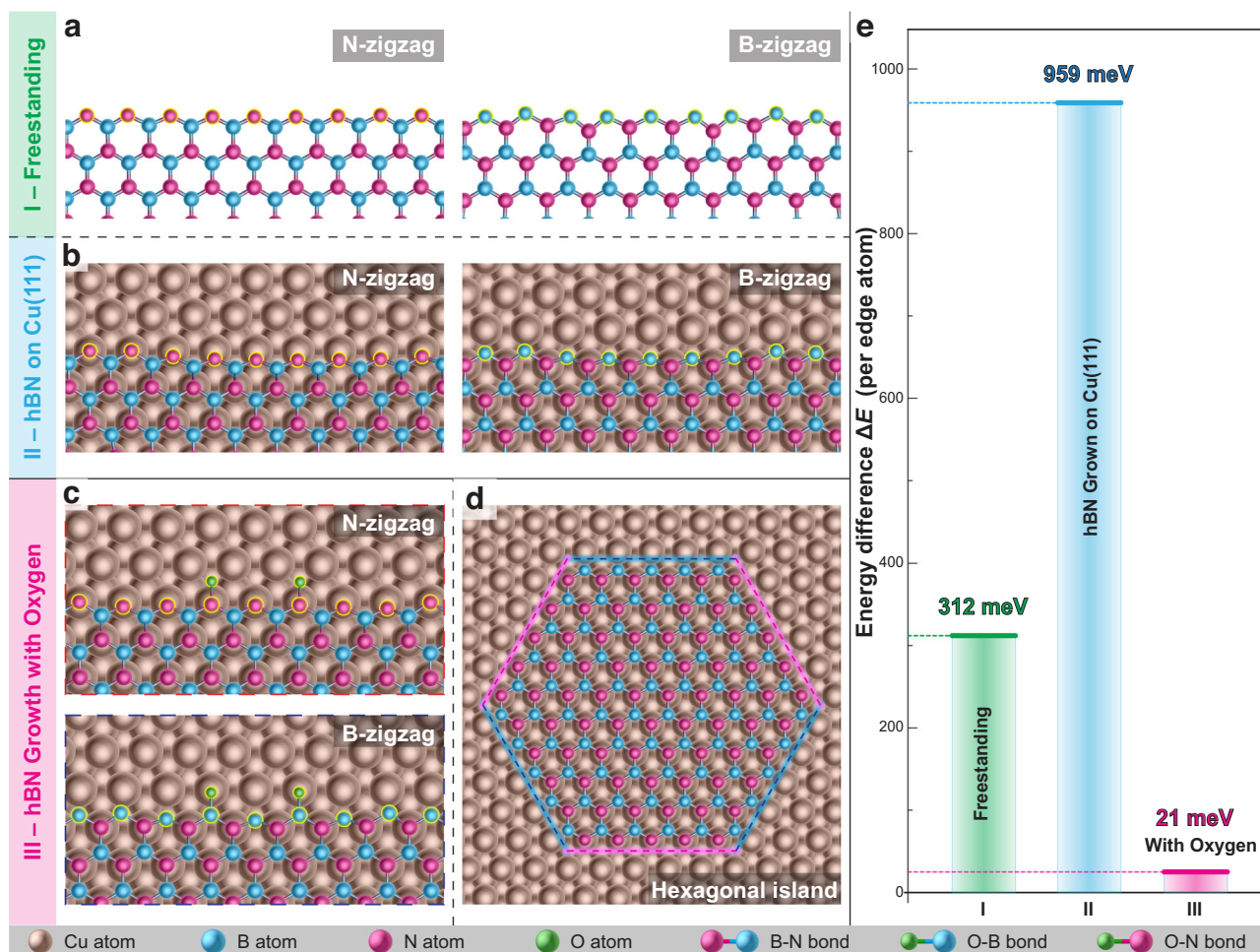


**Fig. 3 | Atomic structures and density functional theory (DFT) simulations.**

**a, b** Atomic structures of relaxed N- (left) and B-terminated (right) zigzag edges of freestanding monolayer hBN (**a**) and monolayer hBN on Cu(111) (**b**). **c** Atomic structures of relaxed N- and B-terminated zigzag edges of monolayer hBN on Cu(111) with a low concentration of attached O atoms. **d** Atomic structure of a

hexagonal monolayer hBN island on Cu(111). The N- and B-terminated zigzag edges are marked in blue and red, respectively. **e** Energy differences between the N- and B-terminated edges (**a**, **b**, and **c**). All images are viewed in the (0001) direction. The O, B, N, and Cu atoms are shown in green, blue, magenta, and brown, respectively.

of opposite-oriented hexagonal islands were further investigated by our DFT simulations. The energy difference between the oppositely oriented hBN hexagonal islands in the surface-growth mode was 0.035 eV, slightly exceeding thermal energy at room temperature ( $\sim 0.026$  eV), compared to 1.041 eV for the step-edge-growth mode (see further discussion in Supplementary Fig. 8). This result suggests that the step-edge growth mechanism likely plays a crucial role in our experimental observation of identically oriented hexagonal-shaped hBN islands while inhibiting the formation of islands with opposite orientations and twin boundaries. These theoretical findings strongly support our experimental results on the formation of well-aligned hexagonal hBN islands.

### Monolayer hBN from hexagonal islands

By adjusting the growth time and parameters of the CVD synthesis, the well-aligned hexagonal islands can merge and eventually form high-quality single-crystal monolayer hBN films on Cu(111) foils (Fig. 4a). The nucleation densities and grain sizes of as-grown hBN islands were controllable, as shown in the SEM images (Fig. 4b–d). A single-crystal Cu(111) substrate is crucial for the synthesis of a large-area single-crystal hBN film. Large-area SEM images and electron backscatter diffraction (EBSD) inverse pole figure (IPF) maps of normal and in-plane directions prove single crystallinity without twin grains of our Cu(111) foils (Supplementary Figs. 9 and 10). Consequently, a  $25 \times 70$  mm<sup>2</sup>

single-crystal monolayer hBN film from hexagonal islands was grown on this type of Cu(111) foil (Fig. 4e). X-ray photoelectron spectroscopy (XPS) was used to analyze the chemical composition of the as-grown hBN film on the Cu(111) foil. High-resolution XPS spectra of the B 1s and N 1s core levels were obtained at 190.6 eV and 398.2 eV, respectively, assigned to hBN in agreement with the reported values<sup>39–41</sup> (Fig. 4f, g). Furthermore, by transferring the hBN film onto SiO<sub>2</sub>/Si substrates, a homogeneous contrast in the optical image was observed (Fig. 4h). The typical Raman map of the  $E_{2g}$  band intensity exhibited a uniform monolayer of the hBN film (Fig. 4i). A sharp  $E_{2g}$  band at 1369 cm<sup>-1</sup> with an FWHM  $\sim 15$  cm<sup>-1</sup> was obtained in the Raman spectrum, indicating the good crystal quality of as-grown hexagonal-island-merged monolayer hBN film (Fig. 4j).

### Characterization of single-crystal hBN

We transferred the produced hBN film onto transmission electron microscopy (TEM) grids, and high-resolution TEM (HRTEM) images show excellent crystal quality of the hexagonal-island-merged hBN monolayer (Fig. 5a). Atomically resolved HRTEM images clearly show the honeycomb lattice structure of our monolayer hBN (Fig. 5b). The N and B atoms have different intensities—they can thus be readily identified in HRTEM image (Fig. 5c and Supplementary Fig. 11). A series of large-area HRTEM images were acquired from random locations spanning the entire 3-mm TEM grid, and the correct hBN atomic

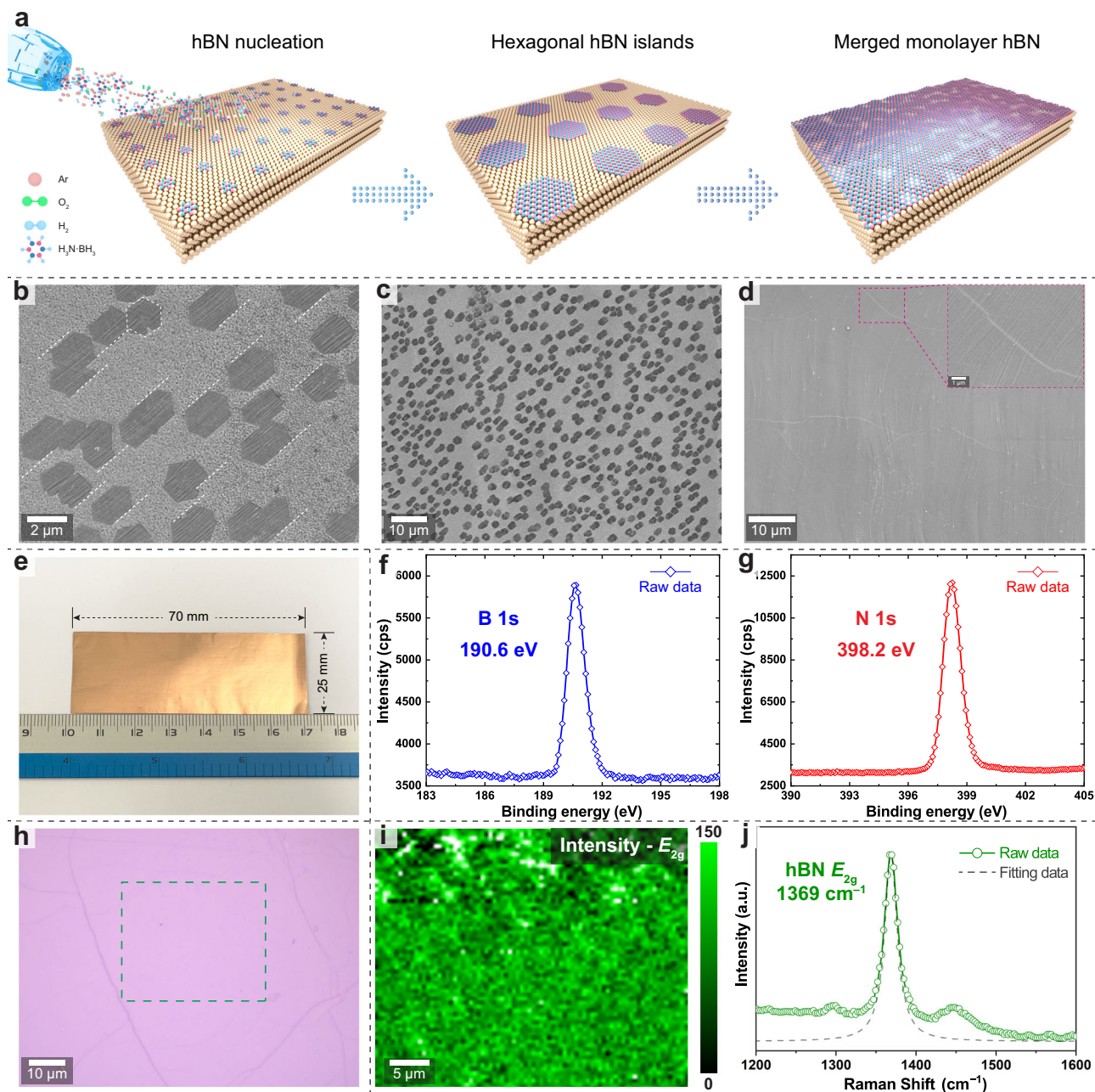


**Fig. 4 | High-quality hexagonal-island-merged monolayer hBN on Cu(111) substrates.** **a** Schematic of the growth process of monolayer hBN merged from well-aligned hexagonal-shaped hBN islands in oxygen-assisted chemical vapor deposition (CVD) synthesis. **b–d** SEM images of the as-grown hBN film showing hexagonal-shaped islands (**b**, **c**), with white dashed lines indicating the alignment of the hexagonal islands, and a fully merged, continuous monolayer hBN film (**d**) on Cu(111) foil. The inset in (**d**) is a magnified view of the hBN wrinkle area. **e** Photograph of as-

grown single-crystal monolayer hBN on Cu(111) foil with areas of  $25 \times 70 \text{ mm}^2$ . **f**, **g** X-ray photoelectron spectroscopy (XPS) spectra measured on as-grown hexagonal-island-merged monolayer hBN film on Cu(111) substrate. **h** Optical image of the as-grown monolayer hBN after transferring onto 90 nm  $\text{SiO}_2/\text{Si}$  substrates. **i** Raman map of the intensity of the hBN  $E_{2g}$  band measured on the marked region in (**h**). **j** Typical Raman spectrum of as-grown hexagonal-island-merged hBN film after transferring onto  $\text{SiO}_2/\text{Si}$  substrates.

arrangement was always obtained with atomic resolution, as shown in Supplementary Fig. 12. Such uniform regular B- and N-atom arrangement without grain boundaries and defects strongly indicates the high crystal quality and low defect density of the monolayer hBN from the hexagonal islands.

Selected area electron diffraction (SAED) patterns acquired at various locations show the same orientation, which confirms that the as-grown hBN is a single-crystal monolayer (Fig. 5d). In addition, a series of HRTEM images and corresponding fast Fourier transform (FFT) patterns were acquired at random locations spanning the entire 3-mm diameter TEM grid. All FFT patterns show the orientation

difference within  $\pm 1^\circ$ , further proving the single-crystal nature of the as-grown hBN monolayer (Supplementary Fig. 13). Cross-sectional TEM image shows a monolayer hBN film and its continuous coverage on the underlying Cu foil (Fig. 5e). The elemental mapping of this interface, conducted through the electron energy loss spectroscopy (EELS), reveals a homogeneous distribution of the as-grown hBN monolayer (Fig. 5f).

### Potential applications

The morphology engineering study of hBN is one of the key roles in understanding the underlying physical mechanism of large-area

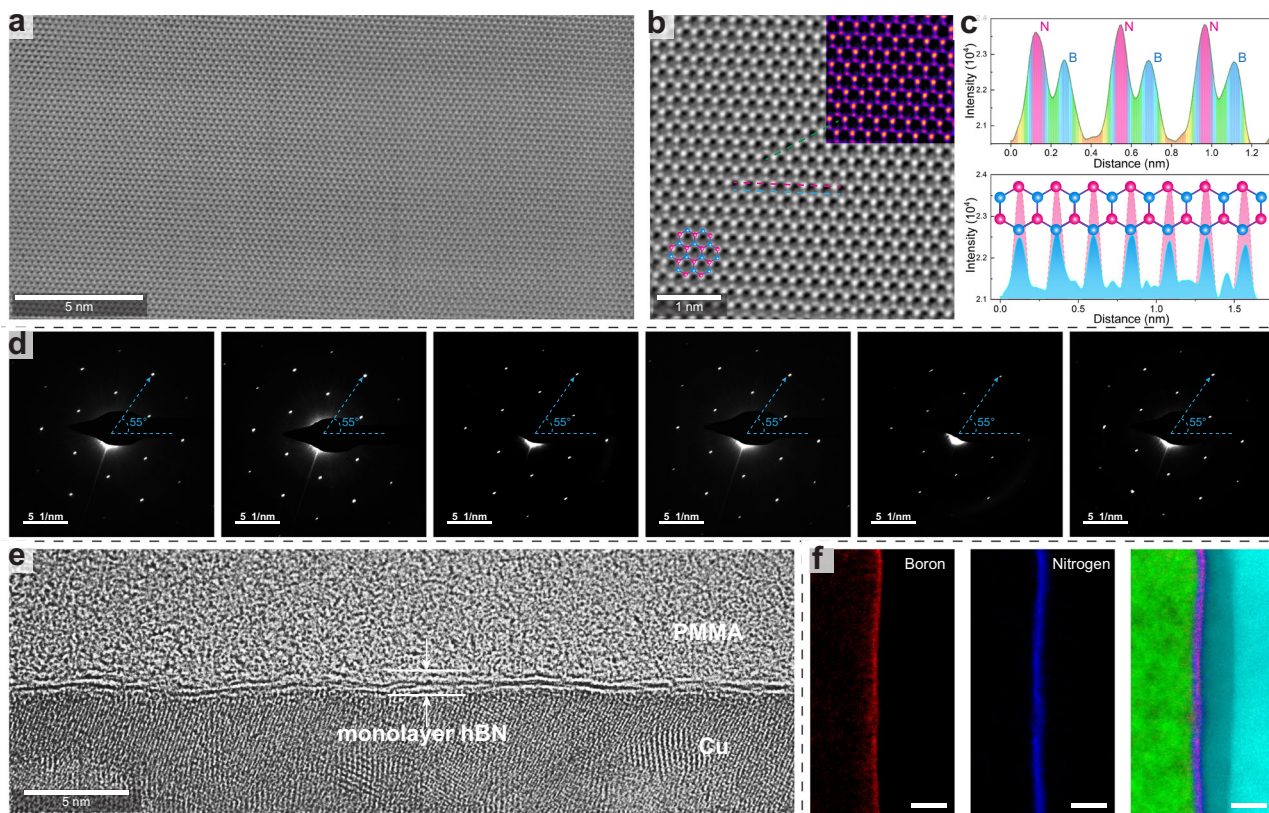


**Fig. 5 | Transmission electron microscopy (TEM) characterization of single-crystal monolayer hBN films.** **a** Large-scale high-resolution TEM image of hexagonal-island-merged monolayer hBN film. **b** Atomic-resolution TEM image of the monolayer hBN film. The inset shows the corresponding false-color image. The red and blue spheres indicate N and B atoms, respectively. **c** Intensity profile along dashed lines in **(b)** with colors of green (upper panel), red and blue (below panel). **d** A series of representative selected area electron diffraction (SAED) patterns

acquired from six random positions across the 3-mm TEM grid. The blue lines indicate the lattice orientation of various locations shows no difference over the entire grid. Scale bars, 5 nm<sup>-1</sup>. **e** Cross-sectional TEM image of the as-grown monolayer hBN film. **f** Electron energy loss spectroscopy (EELS) mappings of the polymethyl methacrylate (PMMA)/hBN/Cu interface from different locations. Scale bars, 5 nm.

single-crystal hBN films with high crystal quality through the CVD growth. In this study, a small concentration of oxygen was deliberately introduced into the CVD growth, and it was found to change the shape of hBN islands (to hexagons rather than triangles) grown on Cu(111). All hexagonal islands evidently merged to form large-area single-crystal monolayer hBN, exhibiting exceptional film quality with a pinhole-free structure and extremely low defect density. This work could accelerate the CVD synthesis of wafer-scale hBN van der Waals heterostructures and facilitate future applications of monolayer hBN in high-reliability electronic devices.

## Methods

### Growth and transfer of hBN

Conventional triangle-shaped hBN was fabricated in a CVD growth system at a growth temperature of 1050 °C using a precursor of ammonia borane (H<sub>3</sub>N–BH<sub>3</sub>, 95%, Sigma-Aldrich). Gas flows of H<sub>2</sub> (10 sccm) and Ar (5 sccm) were introduced into the chamber during the hBN growth process. The temperature of the precursor zone was maintained at 85 °C. After growth, the sample was moved to a room-temperature zone and cooled under the same gas environment. For oxygen-assisted CVD of hBN with hexagonal-shaped islands, diluted O<sub>2</sub> (0.01% in Ar, 5 sccm) was inserted into the CVD chamber during the growth process. The same growth temperature and H<sub>2</sub> gas flow were used for the conventional triangle-shaped hBN growth. The hBN was transferred onto a 90 nm SiO<sub>2</sub>/Si substrate using the conventional polymethyl methacrylate (PMMA)-assisted transfer method.

### Characterization

The Raman spectra and maps were obtained by confocal Raman spectroscopy (Alpha 300 R, WITec) with laser wavelengths of 488 nm and 532 nm. Surface morphologies and EBSD characterizations were obtained by SEM (Quattro ESEM, Thermo Fisher Scientific) equipped with the EBSD accessories. Topography and current maps were collected using the conductive AFM (CAFM, Dimension Icon, Bruker). A Si tip (NCHV-A, 125 μm in length, 8 nm in radius) was used for topography map scanning, and a Pt-coated Si tip (CONTV-PT, 450 μm in length, and 25 nm in radius) was used for current map scanning and collecting *I*–*V* curves. The onset voltage (*V*<sub>on</sub>) is a typical figure of merit defined as the minimum voltage at which currents above the noise level (~1 pA) are detected.

TEM analysis of hBN was performed on a double aberration-corrected Titan Themis Z (Thermo Fisher Scientific) equipped with a monochromator and GIF Continuum K3 (Gatan, Inc.). High-resolution TEM (HRTEM) images were captured using the Themis Z operating at 80 kV with the assistance of the monochromator. The time series of TEM images were acquired using a Ceta CMOS camera, with each frame exposed for 1 s. Drift correction and frame summing were conducted to improve the signal-to-noise ratio of the images. For the examination of the hBN/Cu interface, a cross-sectional lamella with a thickness of ~30 nm was prepared using a focused ion beam (FIB, Helios G4, Thermo Fisher Scientific). A thin layer of PMMA was initially spin-coated onto the Cu foil to protect the hBN monolayer, followed by the ion-beam-assisted platinum (Pt) deposition. HRTEM and scanning transmission electron microscopy (STEM) imaging of the cross-

sectional lamella were performed on Themis Z operating at 300 kV. The chemical composition of the interface was analyzed using electron energy loss spectroscopy (EELS).

XPS measurements were performed using a Kratos Axis Ultra spectrometer ( $h\nu = 1,486.6$  eV) operating at 75 W, a multichannel plate, and a delay line detector under a vacuum of  $1 \times 10^{-9}$  mbar equipped with a monochromatic Al K $\alpha$  X-ray source. Survey and high-resolution spectra were obtained at fixed analyzer pass energies of 160 eV and 20 eV, respectively. The samples were mounted in the floating mode to avoid differential charging. Charge neutralization was required for all the samples. The binding energies were referenced to the C 1s binding energy of adventitious carbon contamination, which was taken to be 284.8 eV.

### DFT simulations

We used density functional theory to investigate monolayer hBN islands on Cu(111) (Vienna Ab initio simulation package)<sup>42</sup>. The Perdew–Burke–Ernzerhof generalized gradient approximation was adopted for the exchange–correlation function. A van der Waals correction was implemented<sup>43</sup>. The energy cut-off of the plane-wave expansion was set to 500 eV. The Brillouin zone was sampled on a  $2 \times 2 \times 1$   $k$ -mesh, and a force convergence criterion of 0.01 eV/Å was used in the structure optimizations. Monolayer hBN was considered on top of a two-layer slab of Cu(111) ( $12 \times 12 \times 1$  supercell; 288 Cu atoms) with the B and N atoms relaxed and the Cu atoms fixed to their bulk positions. In the surface-growth and step-edge-growth modes, we modeled a Cu(111) slab with a three-layered structure, having dimensions of  $6 \times 7 \sqrt{3}$  (336 Cu atoms) for the initial configuration and an additional adsorbed fourth layer (360 Cu atoms). All edge Cu atoms, as well as B and N atoms, were fully relaxed, whereas the bottom Cu layers were fixed. The hexagonal hBN island was composed of 27 N and 27 B atoms; in each case, three N edge atoms interacted with the Cu edge. The thickness of the vacuum layer in the slab model was set to 13 Å.

### Data availability

Relevant data supporting the key findings of this study are available within the article and the Supplementary Information file. All raw data generated during the current study are available from the corresponding authors upon request.

### References

1. Watanabe, K., Taniguchi, T. & Kanda, H. Direct-bandgap properties and evidence for ultraviolet lasing of hexagonal boron nitride single crystal. *Nat. Mater.* **3**, 404–409 (2004).
2. Caldwell, J. D. et al. Photonics with hexagonal boron nitride. *Nat. Rev. Mater.* **4**, 552–567 (2019).
3. Rhodes, D., Chae, S. H., Ribeiro-Palau, R. & Hone, J. Disorder in van der Waals heterostructures of 2D materials. *Nat. Mater.* **18**, 541–549 (2019).
4. Li, M.-Y., Su, S.-K., Wong, H.-S. P. & Li, L.-J. How 2D semiconductors could extend Moore's law. *Nature* **567**, 169–170 (2019).
5. Dean, C. R. et al. Boron nitride substrates for high-quality graphene electronics. *Nat. Nanotechnol.* **5**, 722–726 (2010).
6. Novoselov, K. S., Mishchenko, A., Carvalho, A. & Castro Neto, A. H. 2D materials and van der Waals heterostructures. *Science* **353**, aac9439 (2016).
7. Xie, Y. et al. Fractional Chern insulators in magic-angle twisted bilayer graphene. *Nature* **600**, 439–443 (2021).
8. Stepanov, P. et al. Untying the insulating and superconducting orders in magic-angle graphene. *Nature* **583**, 375–378 (2020).
9. Wang, J. I.-J. et al. Coherent control of a hybrid superconducting circuit made with graphene-based van der Waals heterostructures. *Nat. Nanotechnol.* **14**, 120–125 (2019).
10. Chen, G. et al. Signatures of tunable superconductivity in a trilayer graphene moiré superlattice. *Nature* **572**, 215–219 (2019).
11. Mishchenko, A. et al. Twist-controlled resonant tunnelling in graphene/boron nitride/graphene heterostructures. *Nat. Nanotechnol.* **9**, 808–813 (2014).
12. Zhou, X. H. et al. Large-area orientation-controlled growth of hexagonal boron nitride on liquid copper. *ACS Appl. Electron. Mater.* **4**, 6261–6268 (2022).
13. Ma, K. Y. et al. Epitaxial single-crystal hexagonal boron nitride multilayers on Ni (111). *Nature* **606**, 88–93 (2022).
14. Chen, T. A. et al. Wafer-scale single-crystal hexagonal boron nitride monolayers on Cu (111). *Nature* **579**, 219–223 (2020).
15. Wang, L. et al. Epitaxial growth of a 100-square-centimetre single-crystal hexagonal boron nitride monolayer on copper. *Nature* **570**, 91–95 (2019).
16. Bets, K. V., Gupta, N. & Yakobson, B. I. How the complementarity at vicinal steps enables growth of 2D monocrystals. *Nano Lett.* **19**, 2027–2031 (2019).
17. Lee, J. S. et al. Wafer-scale single-crystal hexagonal boron nitride film via self-collimated grain formation. *Science* **362**, 817–821 (2018).
18. Li, J. et al. Growth of polar hexagonal boron nitride monolayer on nonpolar copper with unique orientation. *Small* **12**, 3645–3650 (2016).
19. Jang, A. R. et al. Wafer-scale and wrinkle-free epitaxial growth of single-oriented multilayer hexagonal boron nitride on sapphire. *Nano Lett.* **16**, 3360–3366 (2016).
20. Song, X. J. et al. Chemical vapor deposition growth of large-scale hexagonal boron nitride with controllable orientation. *Nano Res.* **8**, 3164–3176 (2015).
21. Uchida, Y., Iwaizako, T., Mizuno, S., Tsuji, M. & Ago, H. Epitaxial chemical vapour deposition growth of monolayer hexagonal boron nitride on a Cu (111)/sapphire substrate. *Phys. Chem. Chem. Phys.* **19**, 8230–8235 (2017).
22. Tian, B., Li, J., Chen, M., Dong, H. & Zhang, X. Synthesis of AAB-stacked single-crystal graphene/hBN/graphene trilayer van der Waals heterostructures by in situ CVD. *Adv. Sci.* **9**, 2201324 (2022).
23. Steiner, D., Mittendorfer, F. & Bertel, E. Quasiliquid layer promotes hexagonal boron nitride (h-BN) single-domain growth: h-BN on Pt (110). *ACS Nano* **13**, 7083–7090 (2019).
24. Gao, Y. et al. Repeated and controlled growth of monolayer, bilayer and few-layer hexagonal boron nitride on Pt foils. *ACS Nano* **7**, 5199–5206 (2013).
25. Dong, J., Zhang, L., Dai, X. & Ding, F. The epitaxy of 2D materials growth. *Nat. Commun.* **11**, 5862 (2020).
26. Dong, J., Liu, Y. & Ding, F. Mechanisms of the epitaxial growth of two-dimensional polycrystals. *Npj Comput. Mater.* **8**, 1–11 (2022).
27. Sharma, S. et al. Morphology-controlled synthesis of hexagonal boron nitride crystals by chemical vapor deposition. *Cryst. Growth Des.* **16**, 6440–6445 (2016).
28. Stehle, Y. et al. Synthesis of hexagonal boron nitride monolayer: Control of nucleation and crystal morphology. *Chem. Mat.* **27**, 8041–8047 (2015).
29. Tay, R. Y. et al. Growth of large single-crystalline two-dimensional boron nitride hexagons on electropolished copper. *Nano Lett.* **14**, 839–846 (2014).
30. Felter, J., Raths, M., Franke, M. & Kumpf, C. In situ study of two-dimensional dendritic growth of hexagonal boron nitride. *2D Mater.* **6**, 10.1088/2053-1583/ab2926 (2019).
31. Liu, Y., Bhowmick, S. & Yakobson, B. I. BN white graphene with “colorful” edges: The energies and morphology. *Nano Lett.* **11**, 3113–3116 (2011).
32. Wofford, J. M., Nie, S., McCarty, K. F., Bartelt, N. C. & Dubon, O. D. Graphene islands on Cu foils: the interplay between shape, orientation, and defects. *Nano Lett.* **10**, 4890–4896 (2010).
33. Yan, Z., Peng, Z. & Tour, J. M. Chemical vapor deposition of graphene single crystals. *Acc. Chem. Res.* **47**, 1327–1337 (2014).

34. Li, J. et al. Morphology-control growth of graphene islands by nonlinear carbon supply. *Adv. Mater.* **34**, 2206080 (2022).
35. Robertson, A. W. & Warner, J. H. Hexagonal single crystal domains of few-layer graphene on copper foils. *Nano Lett.* **11**, 1182–1189 (2011).
36. Stenger, I. et al. Low frequency Raman spectroscopy of few-atomic-layer thick hBN crystals. *2D Mater.* **4**, 031003 (2017).
37. Cai, Q. et al. Boron nitride nanosheets improve sensitivity and reusability of surface-enhanced Raman spectroscopy. *Angew. Chem.* **128**, 8545–8549 (2016).
38. Chugh, D., Jagadish, C. & Tan, H. Large-area hexagonal boron nitride for surface enhanced Raman spectroscopy. *Adv. Mater. Technol.* **4**, 1900220 (2019).
39. Guimon, C. et al. XPS study of BN thin films deposited by CVD on SiC plane substrates. *Surf. Interface Anal.* **16**, 440–445 (1990).
40. Wang, Q., Li, J., Lin, J. & Jiang, H. Probing the surface oxidation process in hexagonal boron nitride epilayers. *AIP Adv.* **10**, 025213 (2020).
41. Shi, Y. et al. Synthesis of few-layer hexagonal boron nitride thin film by chemical vapor deposition. *Nano Lett.* **10**, 4134–4139 (2010).
42. Kresse, G. & Furthmüller, J. Efficient iterative schemes for ab initio total-energy calculations using a plane-wave basis set. *Phys. Rev. B* **54**, 11169 (1996).
43. Grimme, S., Antony, J., Ehrlich, S. & Krieg, H. A consistent and accurate ab initio parametrization of density functional dispersion correction (DFT-D) for the 94 elements H–Pu. *J. Chem. Phys.* **132**, 154104 (2010).

## Acknowledgements

X.Z. acknowledges support from King Abdullah University of Science and Technology (KAUST), under the Semiconductor Initiative – Emerging Semiconductor Materials Thrust.

## Author contributions

J.L. and B.T. conceived the experiments. B.T. and X.Z. supervised the project. J.L. performed Cu(111) foil fabrication, hBN growth, and transfer experiments. J.L. and B.T. performed the optical, Raman, SEM, and EBSD characterizations. Y.Y. and M.L. performed the AFM and CAFM measurements. M.N.H. and B.T. performed the XPS measurements. Q.W. and B.T. performed the FIB, HRTEM, SAED, and EELS measurements. B.T. designed, assembled, and built the hBN CVD growth system. A.S. and U.S. performed the DFT simulations and theoretical analysis. I.A., D.A.,

and Z.L. discussed and provided comments on the manuscript. J.L. and B.T. wrote the manuscript. All authors revised and commented on the manuscript.

## Competing interests

The authors declare no competing interests.

## Additional information

**Supplementary information** The online version contains supplementary material available at <https://doi.org/10.1038/s41467-024-52944-9>.

**Correspondence** and requests for materials should be addressed to Bo Tian or Xixiang Zhang.

**Peer review information** *Nature Communications* thanks the anonymous reviewers for their contribution to the peer review of this work. A peer review file is available.

**Reprints and permissions information** is available at <http://www.nature.com/reprints>

**Publisher's note** Springer Nature remains neutral with regard to jurisdictional claims in published maps and institutional affiliations.

**Open Access** This article is licensed under a Creative Commons Attribution-NonCommercial-NoDerivatives 4.0 International License, which permits any non-commercial use, sharing, distribution and reproduction in any medium or format, as long as you give appropriate credit to the original author(s) and the source, provide a link to the Creative Commons licence, and indicate if you modified the licensed material. You do not have permission under this licence to share adapted material derived from this article or parts of it. The images or other third party material in this article are included in the article's Creative Commons licence, unless indicated otherwise in a credit line to the material. If material is not included in the article's Creative Commons licence and your intended use is not permitted by statutory regulation or exceeds the permitted use, you will need to obtain permission directly from the copyright holder. To view a copy of this licence, visit <http://creativecommons.org/licenses/by-nc-nd/4.0/>.

© The Author(s) 2024